Large-scale calcium imaging with a head-mount axial scanning 3D fluorescence microscope

Yuichiro Hayashi[1]*, Ko Kobayakawa[1] and Reiko Kobayakawa[1]

[1] Institute of Biomedical Sciences, Kansai Medical University, 2-5-1 Shin-machi, Hirakata, Osaka 573-1010, Japan

* Corresponding author

Correspondence:

Yuichiro Hayashi

Institute of Biomedical Sciences, Kansai Medical University, 2-5-1 Shin-machi, Hirakata, Osaka 573-1010, Japan

e-mail: hayasyui@hirakata.kmu.ac.jp

tel: +81 72 804 2577

Abstract

Miniaturized fluorescence microscopes are becoming more important for deciphering the neural codes underlying various brain functions. Using gradient index (GRIN) lenses, these devices enable the recording of neuronal activity in deep brain structures. However, to minimize any damage to brain tissue and local circuits, the diameter of the GRIN lens should be 0.5–1 mm, which results in a small field of view. Considering the three-dimensional (3D) structure of neural circuits in the brain, volumetric imaging capability would increase the number of neurons imaged through the lenses. To observe 3D calcium dynamics, we developed a miniaturized microscope with an electrically tunable lens. Using this microscope, we performed 3D calcium imaging in behaving mice and were able to image approximately twice the number of cells as could be recorded using a 2D imaging technique. This simple low-cost 3D microscope will improve the efficiency of calcium imaging in behaving animals.

Introduction

Calcium imaging enables researchers to record the activity of hundreds of neurons at cellular resolution simultaneously. In particular, the combination of miniature head-mount microscopes and genetically encoded calcium indicators permits neuronal activity to be tracked for days to months in free-moving small animals (Ghosh et al., 2011; Ziv et al., 2013). For deep brain imaging, gradient index (GRIN) lenses have been used to relay images to microscopes (Ghosh et al., 2011; Jung et al., 2004; Levene et al., 2004; Ziv et al., 2013). However, the implantation of GRIN lenses damages brain tissue. Therefore, to minimize this damage, lenses with a smaller diameter (0.5~1 mm) and small field of view should be used for deep brain imaging. Considering the three-dimensional (3D) structure of neural circuits in the brain, 3D imaging represents a possible strategy for maximizing the number of recorded cells through a limited field of view.

To record 3D fluorescence images from behaving small animals, the use of a light-field imaging-based microscope has been reported (Skocek et al., 2018). This technique maps a 3D image onto an image sensor using a microlens array, and then the 3D image is reconstructed computationally from the two-dimensional (2D) image captured by the image sensor (Levoy et al., 2006). Therefore, its frame rate can be as high as that for 2D imaging. However, the spatial resolution is low because both the spatial and depth data are mapped onto a single image sensor.

Another strategy for 3D imaging is to add a focusing element to the microscope. The electrowetting lens (EWTL) is a small, fast, and lightweight variable focus lens. In combination with a one-or two-photon laser-scanning microscope, EWTL-based 3D imaging systems for use in small animals have been reported (Ozbay et al., 2018, 2015). In these systems, the head-mount optical unit contains only the objective lens and EWTL; the unit is connected with an optical fiber bundle to the laser-scanning device. Therefore, the head-mount unit is lightweight, but the optical fiber bundle limits the spatial resolution of the system. In addition, these systems rely on point scanning, which limits the scan rate of 3D volumes.

Here, we developed a low-cost, easy-to-build fast axial scanning fluorescence microscope based on the EWTL. Using this microscope, we recorded 3D images of

GCaMP6f-expressing neurons from behaving mice and showed that a larger number of neurons could be recorded using 3D imaging than with 2D imaging.

Results

Microscope design

We designed a miniature microscope to capture 3D images from behaving small animals. Because of its accessibility and low cost, the design was based on the UCLA miniscope v3 (miniscope.org). For axial scanning, an EWTL was inserted between the objective lens and the dichroic mirror in the optical path (Figure 1A). The microscope body was 3D-printed to allow rapid prototyping, but the parts could be used repeatedly (Liberti et al., 2017). The weight of the microscope was 3.7 g, which allowed mice to run freely (Figure 1B). We used several types of objective lenses for different applications, and the axial scan range with these lenses was 300~500 μm (Figure 1C, D, Table 1). The aspherical singlet (Asph; Figure 1C, *Left*) is suitable for use with relay optics because of its short length and high numerical aperture. We used tandem achromatic doublets (Ach; Figure 1C, *Right*) to image tissue through a cranial window because of their small tip diameter (2 mm), which made it easier to access the small cranial window on the tissue surface (Figure 4A).

3D imaging in behaving mice

3D imaging is more beneficial for deep brain imaging because the smaller diameter GRIN lens can be used to minimize tissue damage when imaging deeper brain structures. Therefore, we first tested the 3D microscope to image mouse central amygdala (CeA) at ~4 mm below the brain surface through a 0.5-mm-diameter GRIN lens (Figure 2A). Volumetric fluorescence images of GCaMP6f-expressing neurons in CeA were captured at 5 Hz, and each volume image consisted of 12 slices (Figure 2B). However, the first image in the Z-scan sequence was blurry because of the limited scanning speed of the EWTL (Figure 1, Supplement 2). Therefore, 11 of 12 slices were used to reconstruct the 3D image (Figure 2C, D). The calcium activity of individual neurons was extracted using a principal component and individual component analyses (PCA/ICA)-based algorithm (Mukamel et al., 2009). In total, 75 neurons located at

different depths were clearly seen, as shown in Figure 2D. The nearest neighbor distances between the identified neurons were more than 20 μm (Figure 2E). Fluorescence traces extracted from the 3D movie are shown in Figure 2F. To evaluate the merit of the proposed 3D imaging technique, we compared it with conventional 2D imaging. We counted the number of cells detected in the 3D volume (Figure 3A) and each 2D slice (Figure 3B) and found the seventh and eighth slices to contain the largest number of cells (Figure 3B). Thus, approximately twice as many neurons were identified from the 3D image as from a single 2D image (Figure 3C).

To test the versatility of 3D imaging, we then applied this technique to mouse cerebral cortex. A right-angle prism was implanted into the posterior parietal cortex (PPC), and GCaMP6f fluorescence was imaged through the prism (Figure 4A) (Andermann et al., 2013). For this purpose, we used a combination of achromatic doublets as an objective lens (Figure 4A). A total of 129 neurons were extracted from the 3D movie (Figure 4C and 5A). This objective lens offers small tip diameter, and sufficient working distance. Fluorescence traces extracted from the 3D movie are presented in Figure 4E. As shown in Figure 5B, the eighth 2D slice contained the largest number of cells. Thus, the number of cells extracted using 3D imaging was also twice as many as from 2D imaging (Figure 5C).

Although the volume scan rate of 5 Hz was sufficient to detect calcium transients in this study (Figure 2F and 4E), some applications may require higher frame rates. Thus, we recorded 3D images at higher frame rates. Because the maximum frame rate of the image sensor was 60 Hz, the 3D images were captured as 6 slices at 10 Hz (Figure 6) or 4 slices at 15 Hz (Figure 7) from PPC. As for the recording at 5 Hz, the first image in the Z-scan sequence was discarded in both recordings (Figure 1, Supplement 2). At both the scan rates of 10 and 15 Hz, 1.4 times as many neurons were detected in the 3D movie as the 2D movie (Figure 6D and 7D). The 3D shapes of neurons were still reconstructed from the recorded 3D movie captured at 10 Hz (Figure 6B); however, the volumetric image captured at 15 Hz was composed only of 3 slices, which was too few to reconstruct the shapes of the neurons (Figure 7A, B). Although the number of cells detected in the 3D volume was fewer at the higher scan rate than at 5 Hz, 3D imaging at a scan rate of 10 or 15 Hz was still advantageous in terms of cell

numbers compared with 2D imaging (Figure 6D and 7D).

Discussion

3D imaging

In this study, we developed a simple low-cost 3D fluorescence microscope for use in free-moving small animals. Using this microscope, we performed 3D calcium imaging in multiple brain regions, including CeA and PPC (Figure 2 and 4). In these two brain regions, 3D imaging identified approximately twice as many neurons as 2D imaging (Figure 3D and 5D). The 3D technique is particularly advantageous for deep brain imaging because the small diameter GRIN lens is used. We tested several combinations of frame rates and slice numbers per volume of 3D imaging, and the maximum number of neurons was detected with the largest number of slices per scan (imaged at 5 Hz with 12 slices per scan; Figure 5, 6, and 7). The maximum frame rate of the image sensor used in the microscope was 60 Hz, which limited the number of slices at higher scan rates. Using image sensors with higher frame rates will enable the combination of a higher scan rate and larger slice number.

Microscope design

The microscope was made from off-the-shelf optical components, CMOS image sensor electronics designed by an open-source hardware project (UCLA miniscope), and a custom 3D-printed microscope body. These parts were easily available at low cost. Moreover, the 3D-printed parts were fabricated using a consumer-grade 3D printer (Form2; Formlabs). For these reasons, the design was easily tested and modified.

The weight of the microscope potentially affects animal behavior, and therefore must be kept as low as possible. The weight of the microscope designed for this study was 3.7 g, which was acceptable for use in mice. However, the weight will require further reduction to record images from even smaller animals such as zebra finches (Liberti et al., 2017). The new, lightweight version of the UCLA miniscope (miniscope v4; miniscope.org/index.php/Miniscope_v4) will be suitable for use in place of the miniscope v3 to reduce weight. Fortunately, miniscope v4 includes an EWTL in its optical path and can capture 3D images with minimal modification.

Image processing

We used a PCA/ICA-based algorithm to extract individual cell activity from the 3D images (Figure 2D and 4D). A recent report has indicated that CNMF-E, a non-negative matrix factorization-based cell sorting algorithm, performs better for wide-field calcium imaging data than the PCA/ICA-based algorithm (Zhou et al., 2018). The adaptation of the CNMF-E algorithm for use on wide-field 3D imaging data will be an important research theme for the future.

Spatial resolution

The 3D imaging system presented here separated signals from neurons located at different depths (Figure 2D and 4C). However, due to light scattering in the brain tissue and lack of optical sectioning capability in the microscope system, the axial resolution of the 3D microscope was not sufficient to discriminate closely packed small cells. To increase the axial resolution, adding an optical sectioning capability to the miniature microscope system will be an important challenge for the future.

Materials and methods

Head-mount 3D microscope

The miniature microscope design was based on the UCLA Miniscope v3 (miniscope.org). Excitation light was emitted from a blue LED (LXML-PB01-0030; Lumileds, Aachen, Germany). The light passed through an excitation filter (ET470/40x; Chroma Technology, Bellows Falls, VT) and was reflected by a dichroic mirror (T495lpxr; Chroma Technology) onto the tissue through an EWTL (Varioptic A-25H0; Corning, Corning, NY) and an objective lens (aspherical singlet; #83-605, Edmund Optics, Burlington, NJ or tandem configuration of achromatic doublets; #84-126 and #49-271, Edmund Optics). The fluorescent emissions collected by the objective lens were passed through the dichroic mirror and an emission filter (ET525/50m; Chroma Technology). The fluorescence image was focused by a tube lens (#49-277; Edmund Optics) and captured by a CMOS image sensor (MT9V032; ON Semiconductor, Phoenix, AZ). The microscope body was made using a 3D printer (From2, resin type FGPBLK03; Formlabs,

Somerville, MA). The design files are available at https://github.com/yuichirohayashi/Zscope. For deep brain imaging, the image was relayed with a GRIN lens (0.5-mm diameter, 7.9-mm length, 0.61 numerical aperture; CLHS050GFT009; Gofoton, Tsukuba, Japan). The driving voltage for the EWTL (square wave, 2 kHz) was generated using a data acquisition board (PCIe-6259, National Instruments, Dallas, TX) controlled by custom software written in LABVIEW 7.1 (National Instruments) and then amplified by a linear amplifier (As-904-150B, NF Corporation, Yokohama, Japan). The EWTL driver was synchronized to image acquisition of the CMOS image sensor (Figure 1, Supplement 1).

Point spread function measurements

The point speed function was measured by imaging 3D stacks of 1-μm fluorescent beads with a spacing of 5 μm. The lateral and axial resolutions were estimated from the full-width at half-maximum of the intensity profile of the point speed function.

Animals

Adult male C57BL/6N mice were purchased from Japan SLC, Inc. (Shizuoka, Japan). The mice were housed under a standard 12-h light/dark cycle and allowed *ad libitum* access to food and water. We used >10-week-old male mice for all experiments. All animal care and use were performed in accordance with the protocols approved by the Animal Research Committee of Kansai Medical University.

Surgery

The animals were anesthetized using isoflurane. The skull was exposed, and small craniotomies (<0.5 mm) were made over the target brain regions. AAV10-syn-GCaMP6f-WPRE (University of Pennsylvania vector core) was diluted to 5×10^{12} particles/mL in phosphate-buffered saline, and 200 nL were injected. The stereotaxic coordinates of the virus injection were follows: CeA, AP −1.1 mm, ML 2.5 mm, DV −4.5 mm; PPC, AP −2.0 mm, ML 1.5 mm, and DV −0.5 mm. One week after the viral injection, the second surgical procedure was carried out to implant the optics. For CeA imaging, we implanted the GRIN lens to target this region and glued it to the

skull with dental cement (Shofu, Kyoto, Japan). For PPC imaging, the mice were implanted with an aluminum-coated right-angle prism (1.0 mm; #66-773; Edmund Optics) in the PPC (Figure 4A). The microprism was attached to a cranial window assembly composed of a glass coverslip (0.12-mm thick) and a stainless-steel cannula (3.4-mm outer diameter, 2.84-mm inner diameter, and 1.0-mm height).

Four weeks after implantation of the optical parts, GCaMP-expressing neurons were imaged using the microscope, and its aluminum baseplate was cemented in a position at which neurons could clearly be seen.

Imaging sessions

The excitation light intensity was approximately 0.1–0.5 mW/mm^2. Images were captured at 60 Hz for 5 min. To prevent missing frames, image data were first stored in the computer's memory before being transferred to the hard drive once image acquisition had been completed.

Image processing

ImageJ 1.52 (National Institutes of Health, MA) and MATLAB 2018a (Mathworks, Natick, MA) were used for all analyses. The lateral displacements of the brain were corrected by image translation using TurboReg (Thévenaz et al., 1998). Spatial filters corresponding to individual cells were identified using a PCA/ICA-based algorithm (Mukamel et al., 2009). The calculated spatial filters were then visually inspected, and those showing non-neuronal morphology were removed.

Acknowledgements

This work is supported by JSPS KAKENHI (Grant No. 17K19436, 20K07715, 20H03547) toYH, JSPS KAKENHI 20H04849 to RK.

Competing interests

The authors declare no conflict of interest.

References

Andermann ML, Gilfoy NB, Goldey GJ, Sachdev RNS, Wölfel M, McCormick DA, Reid RC, Levene MJ. 2013. Chronic cellular imaging of entire cortical columns in awake mice using microprisms. *Neuron* **80**:900–913. doi:10.1016/j.neuron.2013.07.052

Ghosh KK, Burns LD, Cocker ED, Nimmerjahn A, Ziv Y, Gamal A El, Schnitzer MJ. 2011. Miniaturized integration of a fluorescence microscope. *Nat Methods* **8**:871–8. doi:10.1038/nmeth.1694

Jung JC, Mehta AD, Aksay E, Stepnoski R, Schnitzer MJ. 2004. In vivo mammalian brain imaging using one- and two-photon fluorescence microendoscopy. *J Neurophysiol* **92**:3121–3133. doi:10.1152/jn.00234.2004

Levene MJ, Dombeck DA, Kasischke KA, Molloy RP, Webb WW. 2004. In vivo multiphoton microscopy of deep brain tissue. *J Neurophysiol* **91**:1908–1912. doi:10.1152/jn.01007.2003

Levoy M, Ng R, Adams A, Footer M, Horowitz M. 2006. Light field microscopy. *ACM Trans Graph* **25**:924–934. doi:10.1145/1179352.1141976

Liberti WA, Perkins LN, Leman DP, Gardner TJ. 2017. An open source, wireless capable miniature microscope system. *J Neural Eng* **14**:045001. doi:10.1088/1741-2552/aa6806

Mukamel EA, Nimmerjahn A, Schnitzer MJ. 2009. Automated analysis of cellular signals from large-scale calcium imaging data. *Neuron* **63**:747–760. doi:10.1016/j.neuron.2009.08.009

Ozbay BN, Futia GL, Ma M, Bright VM, Gopinath JT, Hughes EG, Restrepo D, Gibson EA. 2018. Three dimensional two-photon brain imaging in freely moving mice using a miniature fiber coupled microscope with active axial-scanning. *Sci Rep*

8:1–14. doi:10.1038/s41598-018-26326-3

Ozbay BN, Losacco JT, Cormack R, Weir R, Bright VM, Gopinath JT, Restrepo D, Gibson EA. 2015. Miniaturized fiber-coupled confocal fluorescence microscope with an electrowetting variable focus lens using no moving parts. *Opt Lett* **40**:2553–2556. doi:10.1364/ol.40.002553

Skocek O, Nöbauer T, Weilguny L, Martínez Traub F, Xia CN, Molodtsov MI, Grama A, Yamagata M, Aharoni D, Cox DD, Golshani P, Vaziri A. 2018. High-speed volumetric imaging of neuronal activity in freely moving rodents. *Nat Methods* **15**:429–432. doi:10.1038/s41592-018-0008-0

Thévenaz P, Ruttimann UE, Unser M. 1998. A pyramid approach to subpixel registration based on intensity. *IEEE Trans Image Process* **7**:27–41. doi:10.1109/83.650848

Zhou P, Resendez SL, Rodriguez-Romaguera J, Jimenez JC, Neufeld SQ, Stuber GD, Hen R, Kheirbek MA, Sabatini BL, Kass RE, Paninski L. 2018. Efficient and accurate extraction of in vivo calcium signals from microendoscopic video data. *Elife* **7**:1–37. doi:10.7554/eLife.28728

Ziv Y, Burns LD, Cocker ED, Hamel EO, Ghosh KK, Kitch LJ, El Gamal A, Schnitzer MJ. 2013. Long-term dynamics of CA1 hippocampal place codes. *Nat Neurosci* **16**:264–266. doi:10.1038/nn.3329

Figure legends

Figure 1 with 2 supplements

3D fluorescence microscope

(A) Section diagram of a 3D microscope. **(B)** Photo of a mouse with the 3D microscope.

(C) Two types of objective lenses. *Left,* aspherical singlet (Asph). The tip diameter is 4 mm. *Right,* two achromatic doubles in tandem (Ach). The tip diameter is 2 mm. **(D)** The relationship between the driving voltage and the depth of focus.

Figure 1–Figure supplement 1

The wiring diagram for the 3D microscope system. The driving signal of the EWTL was triggered by the synchronized signal from the UCLA miniscope data acquisition box.

Figure 1–Figure supplement 2

Captured image for each Z-slice at the frame rate of 60 Hz. Because of the limited response time of the EWTL, the first frame of the Z-scan sequence was blurred. **(A)** The experimental configuration. A 0.5-mm right-angle prism was imaged with the 3D microscope equipped with the tandem achromatic objective lens. **(C)** Images captured at a volume scan rate of 5 Hz. **(D)** Images captured at a volume scan rate of 10 Hz. **(E)** Images captured at a volume scan rate of 15 Hz.

Figure 2

Three-dimensional fluorescence calcium imaging in a behaving mouse

(A) Anatomical scheme of optical path. A GRIN lens (0.5-mm diameter, 7.9-mm length) was inserted above the CeA. **(B)** Sequence of image acquisition. The solid line indicates the driving signal for the ETWL. The dashed line indicates the actual depth of focus. **(C)** *Upper,* averaged image for each Z-slice. *Lower,* standard deviation of each Z-slice. **(D)** *Left,* volumetric image composed of 11 slices. *Right,* spatial filters representing individual neurons detected by the PCA/ICA algorithm. The contours of 80% of the peak values of each spatial filter are displayed. **(E)** A histogram of the nearest neighbor distance between the neurons shown in (D). **(F)** Fluorescence traces extracted from the 3D movie using spatial filters shown in (D).

Figure 3

Comparison between 3D and 2D imaging from CeA

(A) The orthogonal projection of the 3D spatial filters. **(B)** Contours of spatial filters in

each Z-slice. The number of cells in each Z-slice is shown on right bottom. **(C)** Comparison of the number of cells extracted from the 3D and 2D images.

Figure 4

3D calcium imaging from mouse cerebral cortex using a microprism

(A) The anatomical scheme of the optical path. A 1-mm right-angle prism was inserted in the PPC. **(B)** *Upper,* averaged image for each Z-slice. *Lower,* standard deviation of each Z-slice. **(C)** Spatial filters representing individual neurons detected by the PCA/ICA algorithm. The contours of 80% of the peak values of each spatial filter are displayed. **(D) A** histogram of the nearest neighbor distance between the neurons shown in (C). **(E)** Fluorescence traces extracted from the 3D movie using spatial filters shown in (C).

Figure 5

Comparison between 3D and 2D imaging from PPC

(A) The orthogonal projection of the 3D spatial filters. **(B)** Contours of spatial filters in each Z-slice. The number of cells in each Z-slice is shown on the right bottom. **(C)** Comparison of the number of cells extracted from the 3D and 2D images.

Figure 6

3D imaging at the volume scan rate of 10 Hz

(A) Spatial filters representing individual neurons detected by the PCA/ICA algorithm. The contours of 80% of the peak values of each spatial filter are displayed. **(B)** The orthogonal projection of the 3D spatial filters. **(C)** Comparison of the number of cells extracted from the 3D and 2D images.

Figure 7

3D imaging at the volume scan rate of 15 Hz

(A) Spatial filters representing individual neurons detected by the PCA/ICA algorithm. The contours of 80% of the peak values of each spatial filter are displayed. **(B)** The orthogonal projection of the 3D spatial filters. **(C)** Comparison of the number of cells

extracted from the 3D and 2D images.

Table 1

Optical parameters of the objective lenses

	Focal Length	Numerical Aperture	Working Distance	Lateral PSF FWHM (μm)	Axial PSF FWHM (μm)
Aspherical (Asph)	2.72	0.42	2.23	1.7	21.9
Tandem Achromatic Doublets (Ach)	3.55	0.35	1.42	1.9	15.9

Focal length, numerical aperture, and working distance were calculated using OpTaliX version 8.70 software.

FWHM = full-width at half-maximum; PSF = point spread function

Figure 1

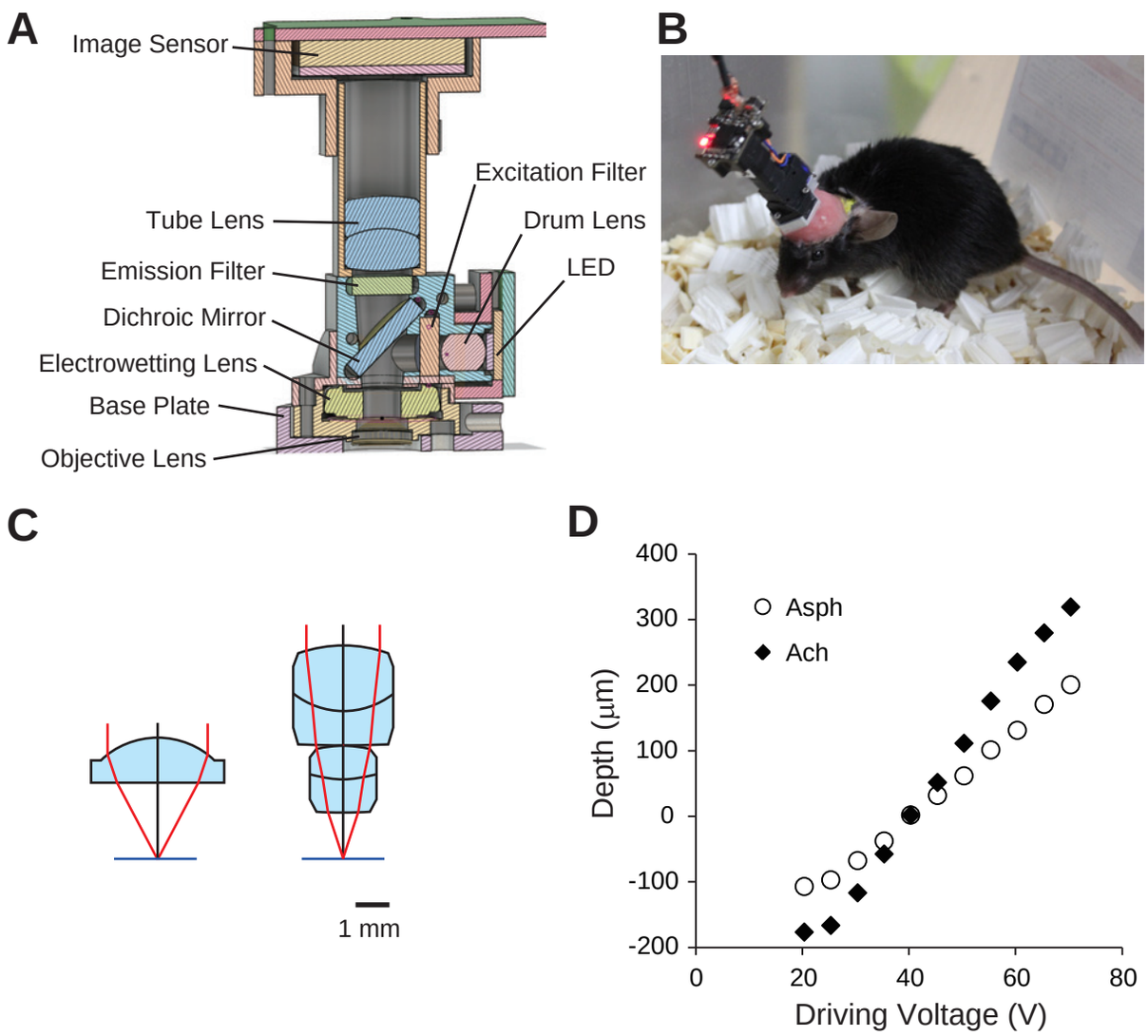
A
Image Sensor
Excitation Filter
Tube Lens
Drum Lens
Emission Filter
LED
Dichroic Mirror
Electrowetting Lens
Base Plate
Objective Lens
B
C
1 mm
D
Asph
Ach
Depth (µm)
400
300
200
100
0
-100
-200
0
20
40
60
80
Driving Voltage (V)

Figure 1 - Figure supplement 1

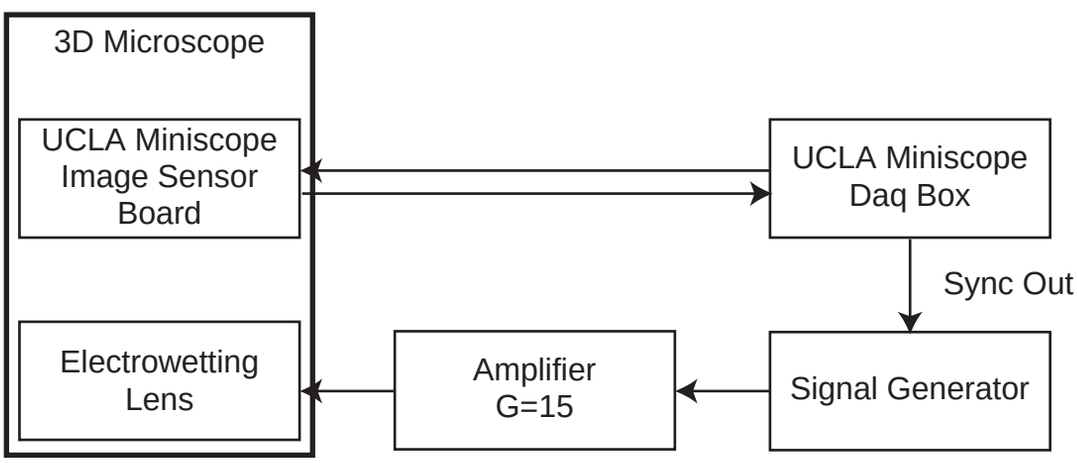

Figure 1 - Figure supplement 2

A

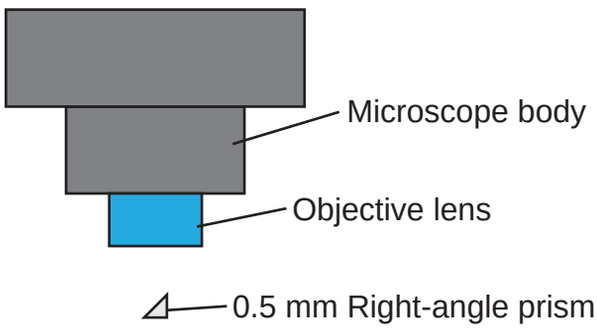

B

5 Hz, 12 slices

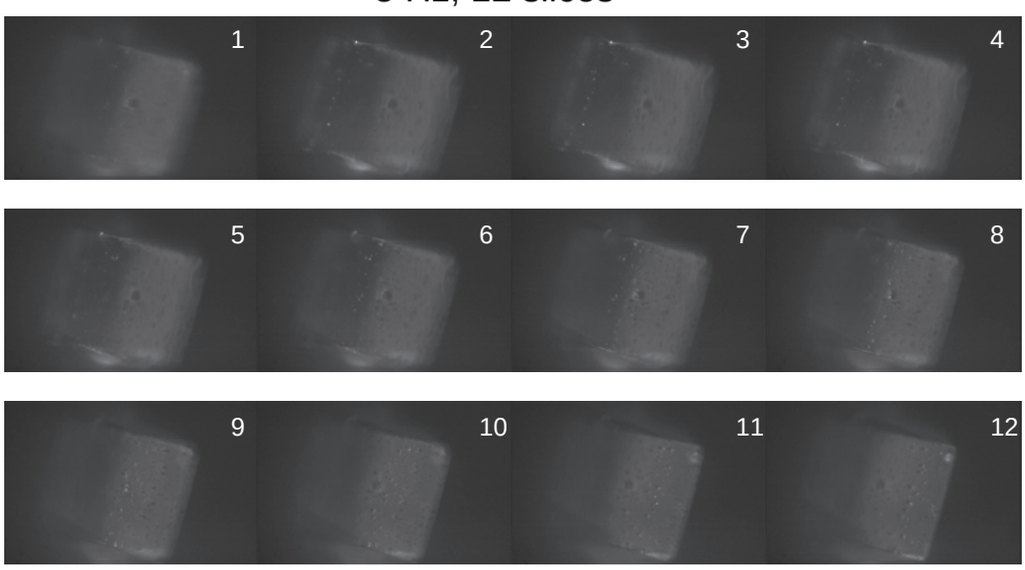

C

10Hz, 6 slices

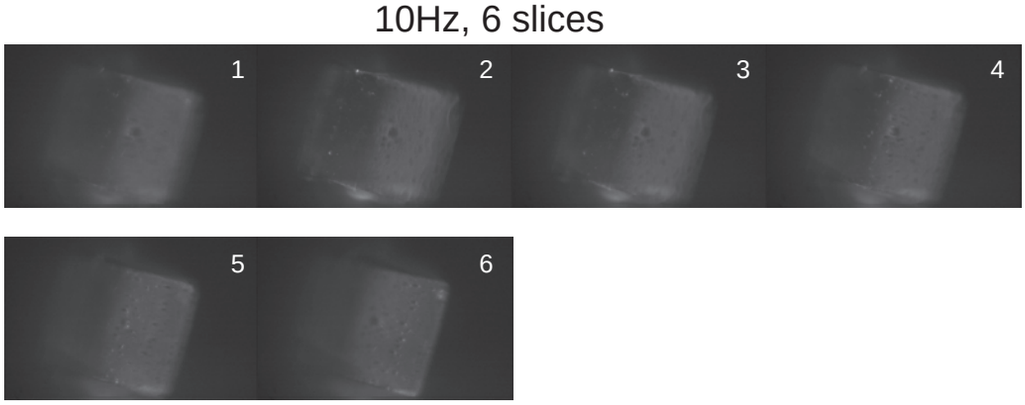

D

15 Hz, 4 slices

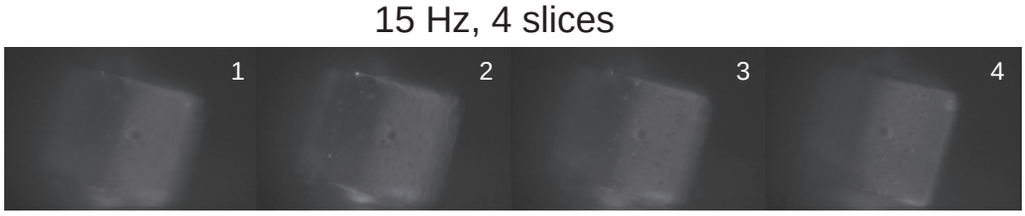

Figure 2

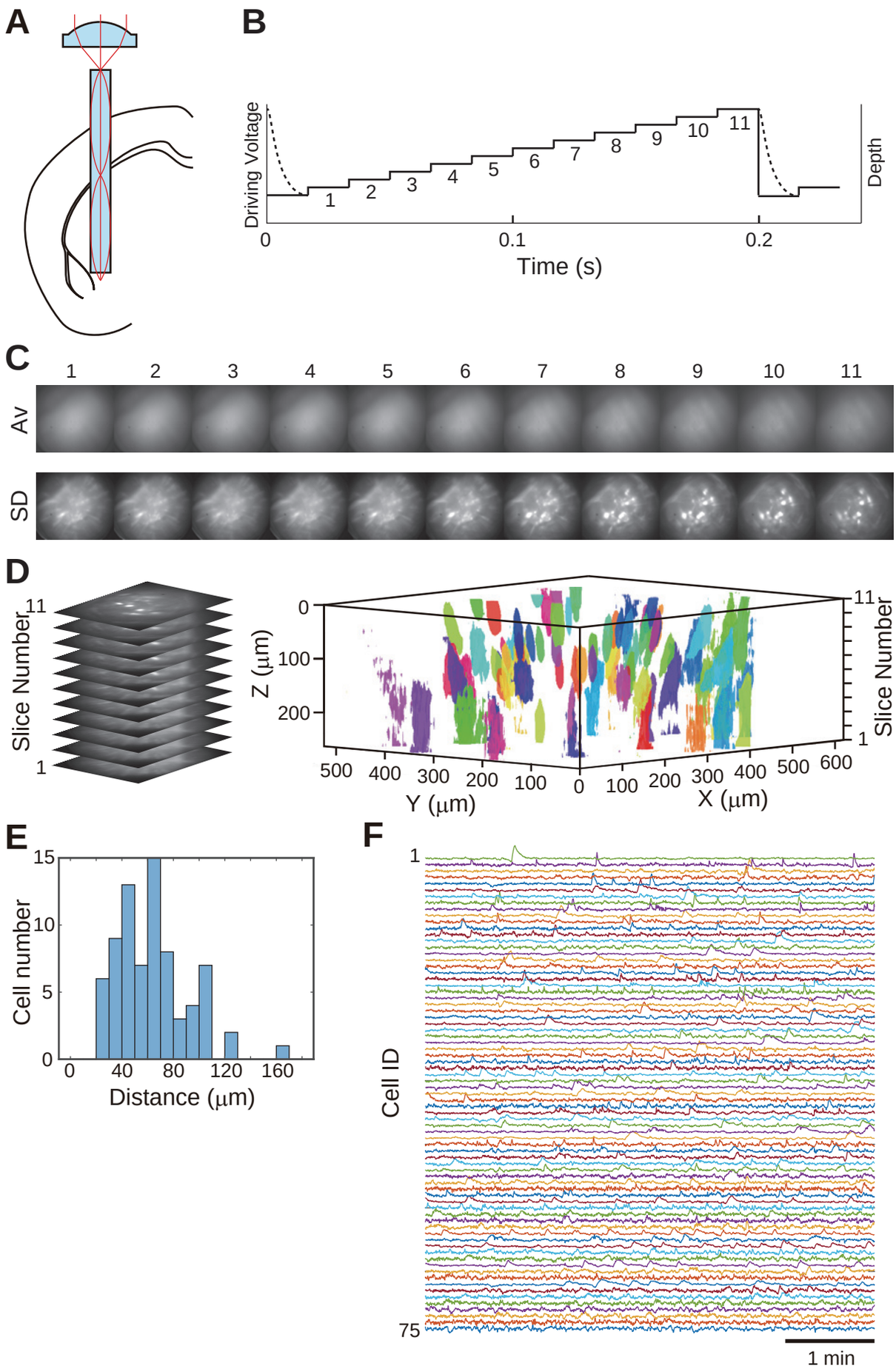
A
B
Driving Voltage
Depth
1
2
3
4
5
6
7
8
9
10
11
0
0.1
0.2
Time (s)
C
Av
SD
D
Slice Number
Z (μm)
Y (μm)
X (μm)
E
Cell number
Distance (μm)
F
Cell ID
1 min

Figure 3

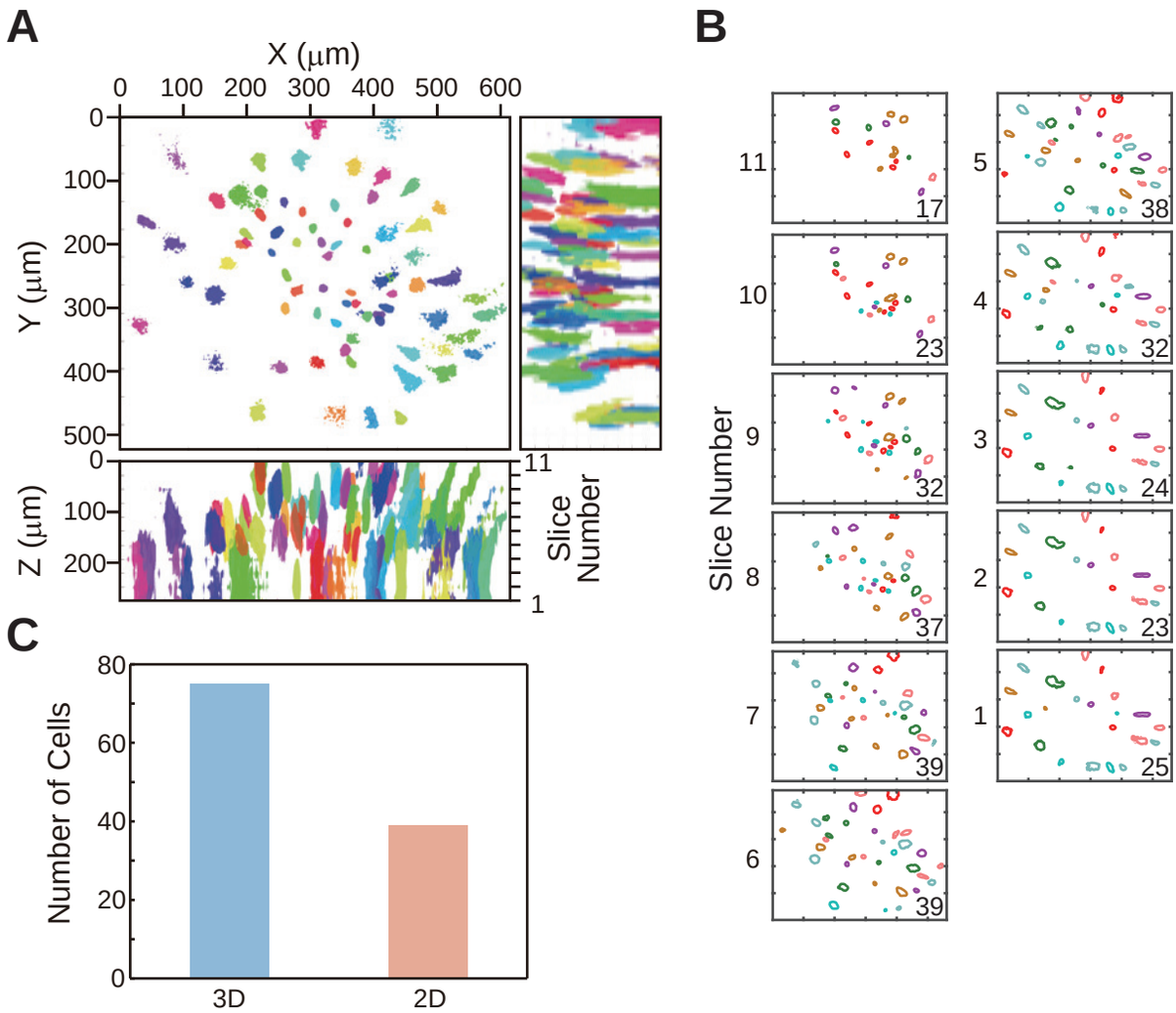
A
X (μm)
0 100 200 300 400 500 600
Y (μm)
0 100 200 300 400 500
Z (μm)
0 100 200
11
1
Slice Number
B
Slice Number
11 17
10 23
9 32
8 37
7 39
6 39
5 38
4 32
3 24
2 23
1 25
C
Number of Cells
80 60 40 20 0
3D
2D

Figure 4

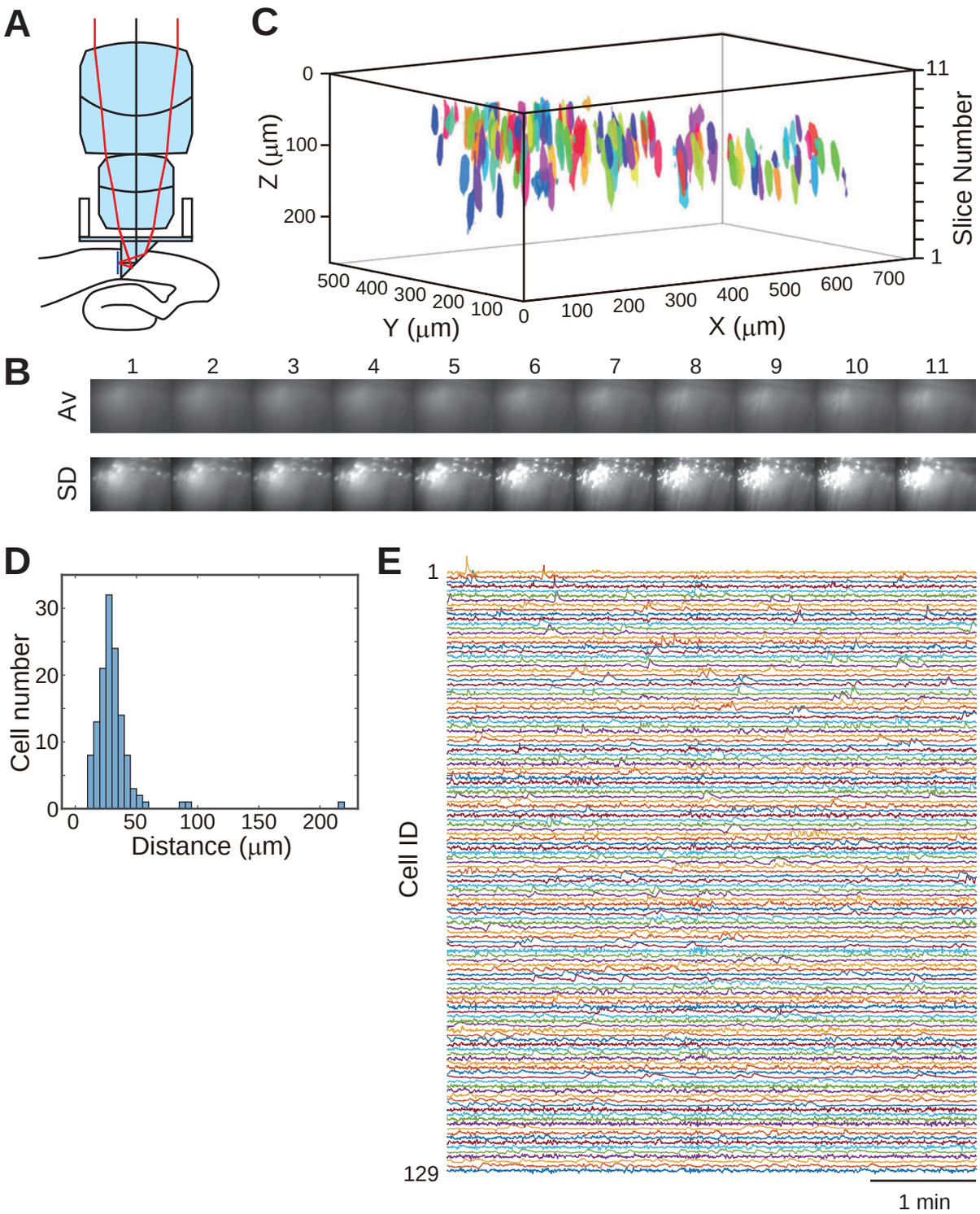
A
C
0
100
200
Z (μm)
11
1
Slice Number
500 400 300 200 100 0
Y (μm)
100 200 300 400 500 600 700
X (μm)
B
1 2 3 4 5 6 7 8 9 10 11
Av
SD
D
30
20
10
0
Cell number
0 50 100 150 200
Distance (μm)
E
1
Cell ID
129
1 min

Figure 5

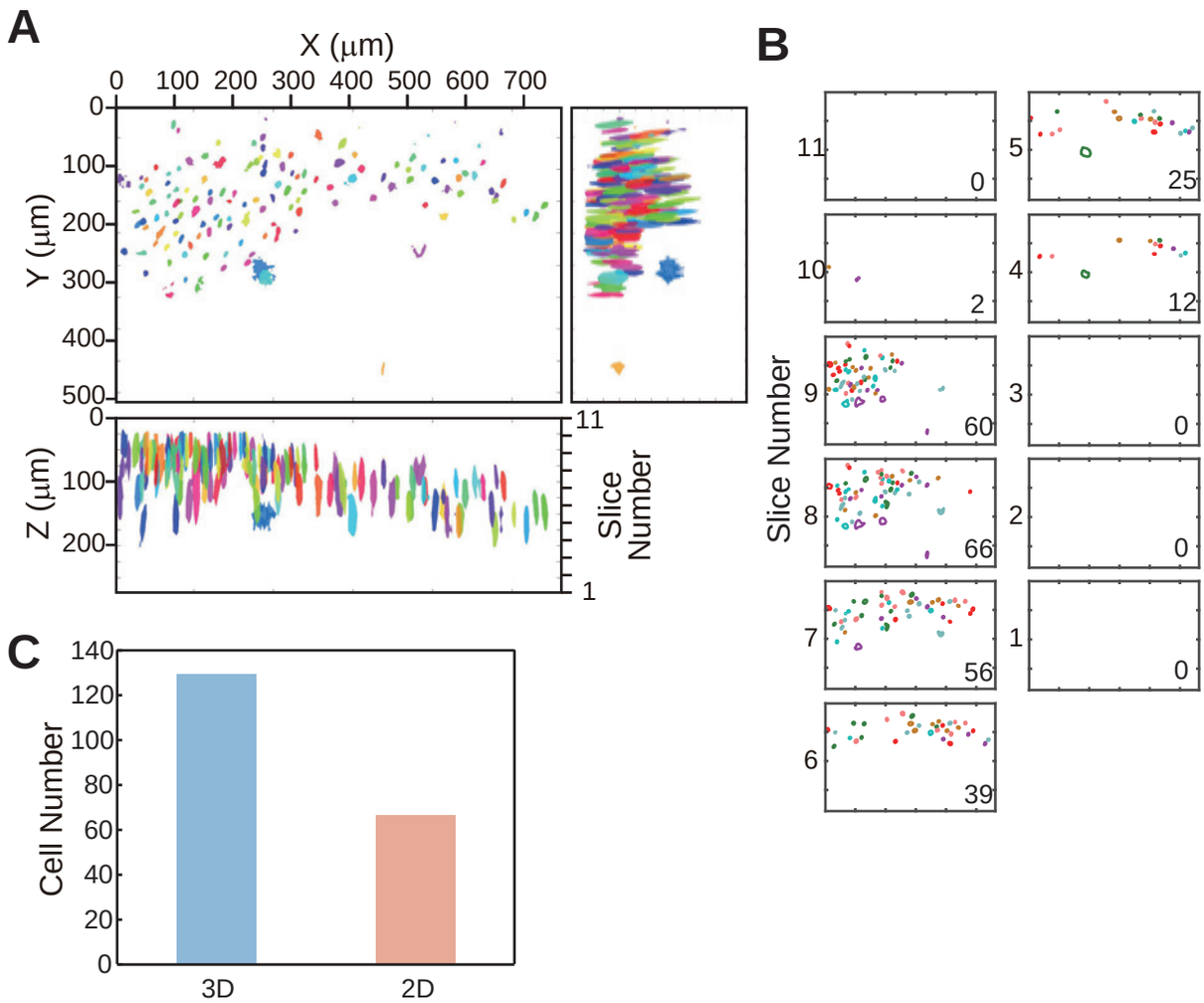
A
X (μm)
0 100 200 300 400 500 600 700
Y (μm)
0 100 200 300 400 500
Z (μm)
0 100 200
11
1
Slice Number
B
Slice Number
11 0
5 25
10 2
4 12
9 60
3 0
8 66
2 0
7 56
1 0
6 39
C
Cell Number
0 20 40 60 80 100 120 140
3D
2D

Figure 6

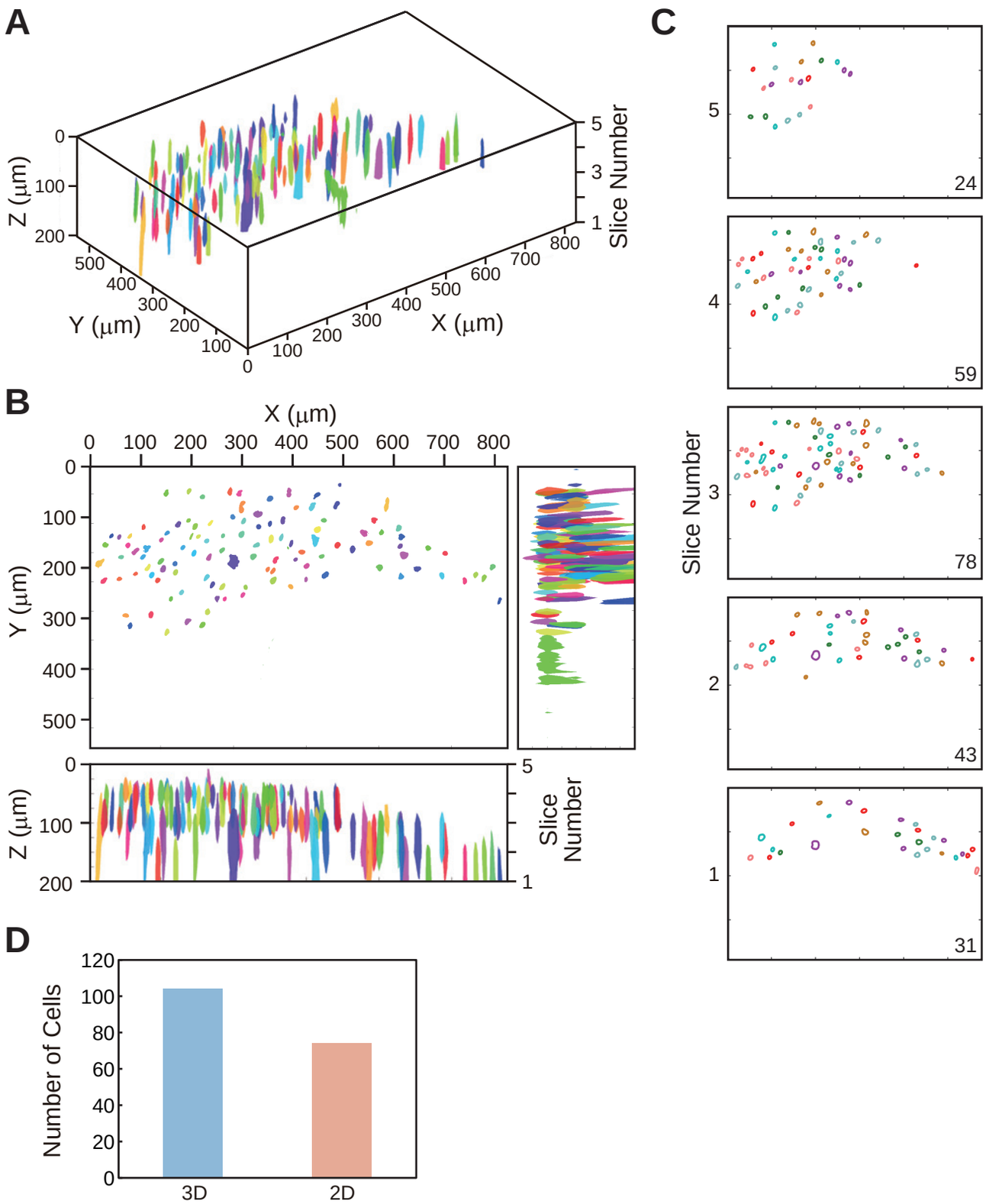
A
Z (μm)
0
100
200
Y (μm)
500
400
300
200
100
0
X (μm)
100
200
300
400
500
600
700
800
Slice Number
5
3
1
B
X (μm)
0 100 200 300 400 500 600 700 800
Y (μm)
0
100
200
300
400
500
Z (μm)
0
100
200
Slice Number
5
1
C
Slice Number
5
24
4
59
3
78
2
43
1
31
D
Number of Cells
120
100
80
60
40
20
0
3D
2D

Figure 7

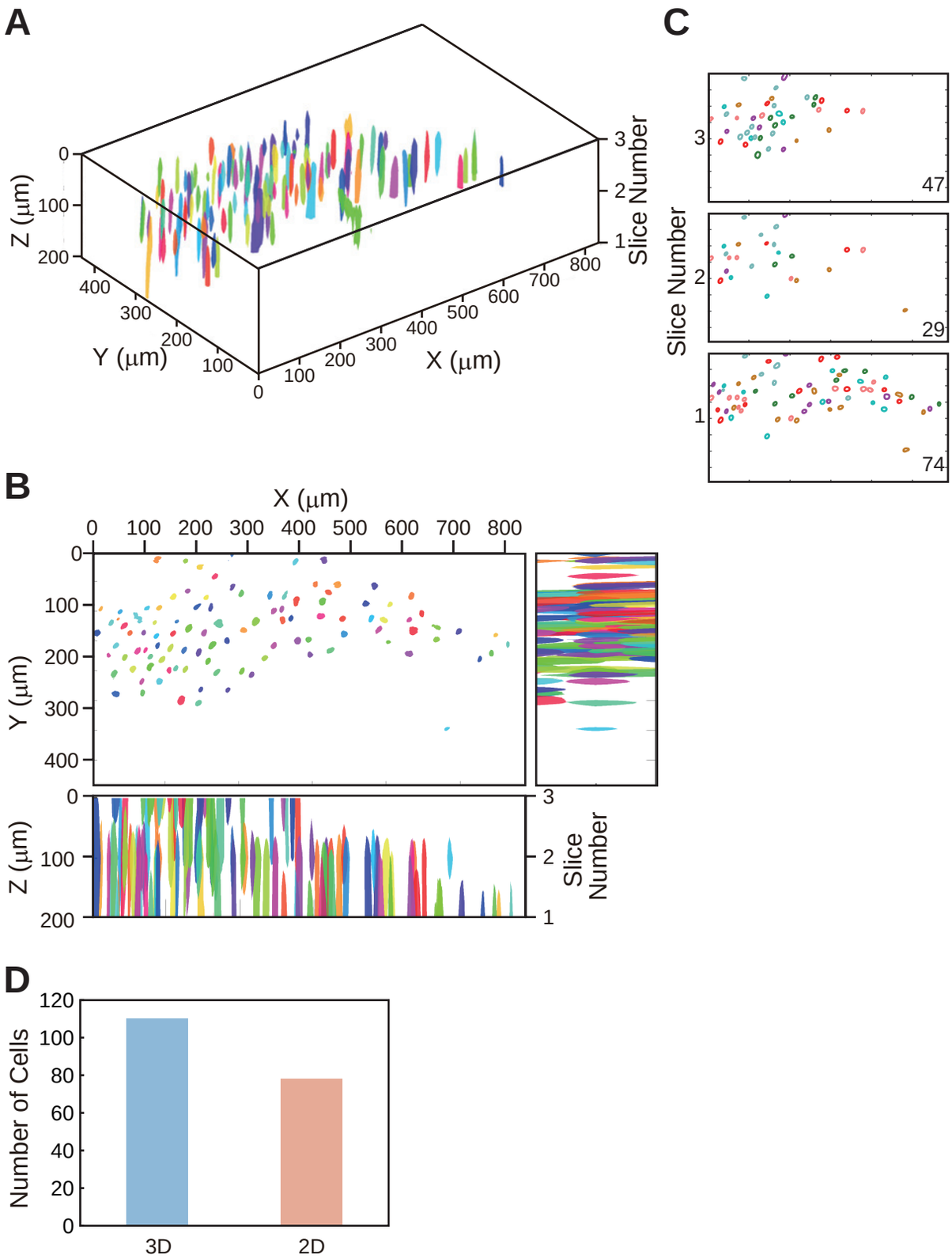
A
Z (μm)
0
100
200
Y (μm)
400
300
200
100
0
X (μm)
100
200
300
400
500
600
700
800
Slice Number
3
2
1
C
Slice Number
3
47
2
29
1
74
B
X (μm)
0 100 200 300 400 500 600 700 800
Y (μm)
0
100
200
300
400
Z (μm)
0
100
200
Slice Number
3
2
1
D
Number of Cells
120
100
80
60
40
20
0
3D
2D